AEOLIAN TONE LEVEL AS A CONSEQUENCE OF DISTANCE TO THE ONSET OF UNSTEADINESS: INFLUENCE OF BLUFF-BODY SHAPE ON THE CRITICAL REYNOLDS NUMBER

Wagner José Gonçalves da Silva Pinto[1] **Florent Margnat**[1] **Camille Noûs**[2]
[1] Institut PPrime, CNRS - Université de Poitiers - ISAE-ENSMA, France
[2] Laboratoire Cogitamus
florent.margnat@univ-poitiers.fr

ABSTRACT

In order to interpret recent results of shape optimization for the aeolian tone problem in 2D, laminar flows, the Reynolds number corresponding to the onset of unsteadiness in a flow over a bluff body is estimated for a set of shapes : five canonical shapes (the ellipse, the rectangle, the losenge and two triangles) are studied, as well as the influence of their aspect ratio that is varied from 0.2 to 2. The critical Reynolds number (Re_c) is obtained by binary search within direct numerical solutions of the Navier-Stokes equations, using Incompact3D solver with an immersed boundary method. A criterion is designed on purpose to discriminate between steady and unsteady solutions. This methodology yields critical Reynolds number values in good agreement with literature results. For all the shapes, Re_c increases exponentially with the aspect ratio. When the latter tends to zero, the evolution for all the shapes merge around $\mathrm{Re}_c \approx 31$, which is that of a flat plate normal to the flow. The ranking of shapes using their Re_c provides insight of the different levels of unsteadiness, and thus of radiated noise, that are noticed between bluff-body flows when analysed at a fixed Reynolds number.

1. INTRODUCTION

Despite numerous efforts in the past, notably from Roskho [1, 2], an universal description of bluff body flow dynamics remains rather empirical and closed models are highly restricted. One fundamental aspect of these dynamics is the transition to unsteadiness. At very slow velocity ($10 \lesssim \mathrm{Re} \lesssim 50$ for the circular cylinder [3], with the Reynolds number defined as $\mathrm{Re} = U_\infty\, d/\nu$, where U_∞ is the free-stream velocity, d is the diameter and ν is the kinetic viscosity), the flow is time independent and defined by a steady re-circulation bubble on the downstream portion of the body. For faster flows, a periodical vortex shedding takes place in what is defined as the Von-Karman instability; the value of the Reynolds number where that transition takes place is referred to as the critical Reynolds number, Re_c.

Several works may be cited in what concerns the transition for the circular section, for instance, [4–6], however, an expanded description of multiple sections is unknown by the authors. Sole examples that could be found in the literature are the studies by Jackson [7] (elliptical sections, a flat plate and isosceles triangle in multiple orientations), Paul *et al.* [8] and Thompson *et al.* [9] (both studies dedicated to elliptical sections of different aspect ratios). We think that including different geometries in the same study is an important path for a better understanding of the flow dynamics. In this work, more than 70 geometries are studied, considering a combination of 5 geometrical paradigms (ellipses, rectangles, and lozenges along with front- and back-pointing triangles) and multiple aspect ratios (ratio between the sectional breadth and height, aspect ratio $\mathrm{AR} = L/d$).

Moreover, studying different aspect ratios is in accordance with the interest given to such kind of geometry modification, notable in aeroacoustics. Modifications of the aspect ratio of rectangular cylinders have been discussed numerically [10–12] and experimentally [13–15]. As stated by Islam *et al.* [16], the streamwise length is an important feature in the definition of the vortex shedding dynamics.

Nevertheless, it has been reported that the amplitude of the flow quantities in terms of wake velocities and integral aerodynamic efforts correlates with the 'distance' of the flow to that transition [4, 17, 18]. This could partly explain the wide range of acoustic efficiency (up to 20 acoustic power dB) noticed in the shape optimizations performed in [19, 20] whereas the blocking height was kept constant.

This paper is organized as follows: the aerodynamic solver and the technique for obtaining the critical Reynolds number are presented and validated in Section 2; next, results for the influence of aspect ratio are presented in Section 3 with a regression model and an estimation of the flat plate critical Reynolds number. Conclusions close the article in Section 4, while some material and discussions are pushed to the Appendix in order to lighten the main text.

2. METHODOLOGY

The critical Reynolds number is binary searched among direct solutions of the unsteady Navier Stokes equations for an interval of Reynolds numbers, using a bisection method driven by a criterion of unsteadiness; the Immersed Boundary Method (IBM) is exploited to simulate many geometries on the same grid. Their implementation is detailed next.

2.1 Solver

The flow is described numerically using an incompressible direct Navier Stokes two-dimensional (2D) solver [21] (DNS). It is a finite difference code with spatial derivatives defined by a 6^{th} order centered scheme and time advancing performed using a 3^{rd} order Runge-Kutta scheme. The pressure field is defined in a sub-step such as to guarantee the incompressibility; the corresponding Poisson equation is solved in the spectral domain.

The mesh is Cartesian, uniform in x and stretched in y direction (points concentrated at the center). The cross-sections are modeled using an Immersed Boundary Method (IBM) [22] to describe the solid domain, generating the following momentum equation for unitary mass:

$$\frac{\partial u_i}{\partial t} + u_j \frac{\partial u_i}{\partial x_j} = -\frac{\partial}{\partial x_j}[p\delta_{ij} - \tau_{ij}] + f_i \qquad (1)$$

where p is the pressure and u_i, δ_{ij}, τ_{ij} and f_i are the components of the velocity vector $\mathbf{u}$, the Kronecker delta, the viscous stress tensor τ and the IBM forcing term $\mathbf{f}$, defined as a damped oscillator [23]:

$$\mathbf{f}(\mathbf{x},t) = -w(\mathbf{x})\left[\omega_n^2 \int_0^t \mathbf{u}(\mathbf{x},t)dt + 2\zeta\omega_n \mathbf{u}(\mathbf{x},t)\right] \qquad (2)$$

The damped system coefficients are selected as ω_n = 50 and ζ = 1, as proposed by Margnat & Morinière [23]. The w matrix drives the spatial weighting of the forcing term: $w = 1$ is set at a grid point located inside the body contour, while $w = 0$ outside (fluid domain). In this application, there are no ghost-cells nor surface-based correction/interpolations, so the shape of the obstacle is limited to the grid resolution. The validation of the present combination of flow solver with IBM technique was conducted specifically for unsteady flows over sharp edged bodies in [23]. Extensive comparisons with literature data were conducted in [11, 19] for aerodynamic integral quantities, that is influence of shape and Reynolds number on Strouhal number, mean drag and lift amplitude.

The numerical setup, as well as the boundary conditions are represented in Figure 1. Current mesh is of $n_x \times n_y = 649 \times 257$ points, for a domain of $25.3d \times 20d$. At inflow, the velocity is set as $[u = U_\infty\ , v = 0]$. At outflow, an open boundary condition is deduced from an explicit, first order approximation of the convection equation:

$$\left.\frac{\partial \mathbf{u}}{\partial t}\right)_{\text{outflow}} + U_\infty \left.\frac{\partial \mathbf{u}}{\partial x}\right)_{\text{outflow}} = \mathbf{0} \qquad (3)$$

The implementation of the boundary conditions in the solver is described in details in [21].

Base timestep duration is of $T = 0.0072\ d/U_\infty$, but due to stability issues of the forcing term, this value is reduced for lower Reynolds number when divergence is encountered, what resulted in a range of 0.0036 to 0.0072 d/U_∞. Time, grid and domain convergence studies have been performed and are presented on earlier works [19,20]. Current parameters allow the complete simulation of a given flow case to be performed within about 2 hours in a single core.

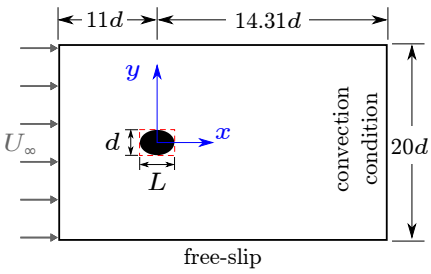

Figure 1. Numerical setup. The aspect ratio is defined as $\mathrm{AR} = L/d$. Sketch not on scale.

2.2 Tested sections

Tested sections are canonical geometries at different aspect ratios. The geometries are rectangle (rect), ellipse (elip), front-pointing isosceles triangle (trif), back-pointing isosceles triangle (trib) and lozenge (losn), as illustrated in Figure 2. All the shapes are symmetric with respect to flow axis. As indicated in Figure 1, the breadth of the shape is noted L and defines the aspect ratio as $\mathrm{AR} = L/d$. Moreover, the height d is the same for all shapes and is the reference length used to form the Reynolds number.

Values of aspect ratio from 0.1 to 2.0 are considered, with an increment of 0.1 for $\mathrm{AR} < 1.0$ and 0.2 otherwise. Intermediary values are also added, associated with the transition of the wake pattern at Re = 150, as discussed in another article [12].

Since an IBM is being used, the description of the obstacle is limited to the precision of the mesh. With the current discretization, each segment d is described by about 25 elements in x and 50 in y.

The numerical setup is quite similar to the work of Paul *et al.* [8] who also studied the Re_c using an IBM based solver. The present contribution extends the discussion to other geometries (more shapes and bigger aspect ratios) and the formal statistical description of the relationship between Re_c and the aspect ratio.

2.3 Estimation of the critical Reynolds number

2.3.1 General principle

Due to the facility of performing multiple simulations in a short time, the chosen strategy for identifying the critical Reynolds number for each geometry is to run successive simulations, the Reynolds number being set by a dichotomy algorithm. Given that all the geometries yield a steady flow at $\mathrm{Re} = 30$, and an unsteady flow at $\mathrm{Re} = 90$, the case $\mathrm{Re} = 60$ is run. If the converged flow is unsteady,

Figure 2. Studied shapes, considering flow from left to right and plotted for $\mathrm{AR} = 1.0$.

then the next run is at the median of the interval $[30, 60]$, that is $\mathrm{Re} = 45$. Otherwise, if the flow is steady, the case $\mathrm{Re} = 75$ is run, and depending on unsteadiness, either the median of the Re interval $[60, 75]$ or $[75, 90]$ will be set for the following step. Thus iterating, a Reynolds number interval, whose lower and upper bounds yield steady and unsteady flow, respectively, is refined until a precision of .5. By design, the onset of unsteadiness is assumed to occurs inside this limit interval.

In order to unman the process, whether the simulated flow is steady or unsteady must be defined with a univocal criterion. As described in the following sections, this requires the selection of a flow quantity, a location where this quantity is monitored, and a threshold.

2.3.2 Settings

After several tests, the fluctuating y-velocity is chosen as the variable of interest for its unanimity in describing the transition in terms of magnitude (fluctuations are bigger than the other flow quantities) and location.

The location of monitoring is set as $(x = 12d, y = 0)$. Indeed, as visible in Figure 3, the unsteady flow sustains non-zero y-velocity in the far wake, whereas the fluid returning the axis after turning around the body yield non-zero y-velocity for $2 \lesssim x/d \lesssim 4$ in the steady regime. Such qualitative difference between the two regimes enables better automatic detection of unsteadiness when monitoring the relative far wake. Placing the probe far from the body also reduces bias due to the shape.

Moreover, on the streamwise axis, the y-velocity is zero by symmetry in both the the steady (before transition) and the mean (after transition) flow, after the transient. This offers better conditions for detecting unsteadiness from a slowly converging steady or mean flow.

For the quantification of unsteadiness, the maximal fluctuation with respect to a moving average is considered. The threshold for defining the unsteadiness is here set to $\Delta v > 10^{-4} U_\infty$ at the end of the simulation (e.g. 25000 timesteps, physical time of $180 d/U_\infty$). This may be compared to the amplitude of physical fluctuations just after the transition, which scales with the following parameter [17, 18, 24]:

$$\varepsilon = \frac{\mathrm{Re} - \mathrm{Re_c}}{\mathrm{Re}_c} \tag{4}$$

The dichotomy final interval being of half a Reynolds number unit, $\mathrm{Re}_c = 50$ leads to $\varepsilon = 0.01$. On the other hand, numerical errors are typically about 10^{-6}. The present threshold is thus very large with respect to residuals and very small with respect to physical fluctuations, so it is relevant to discriminate between both. More details on the selection of this threshold are given in [25].

2.4 Comparison to literature data

The values obtained with the present methodology are now compared to reported Re_c for three canonical shapes at $\mathrm{AR} = 1.0$. For the circular section (Table 1), the dichotomy leads to $\mathrm{Re}_c = 47.3 \pm 0.25$ while the literature interval is [45-48.3]. Most recent studies report $\mathrm{Re}_c \approx 47$.

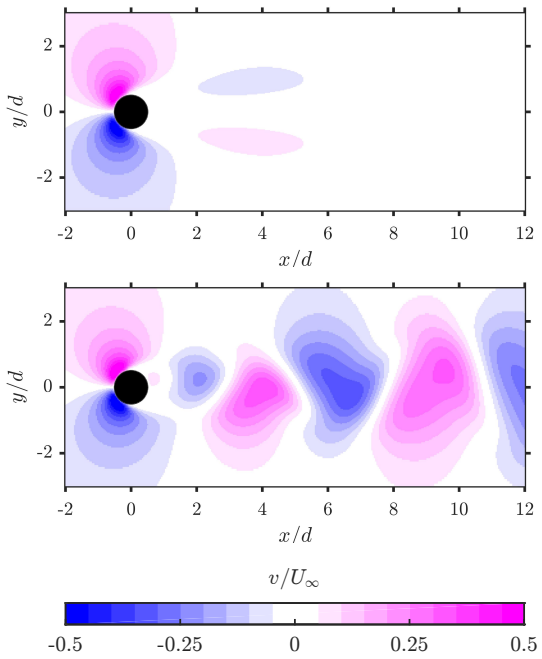

Figure 3. Instantaneous y-velocity fields for a steady (upper, $\mathrm{Re} = 40$) and unsteady (lower, $\mathrm{Re} = 60$) flow, circular cylinder (elip, $\mathrm{AR} = 1.0$).

Table 1. Literature values of Re_c (transition from steady to unsteady flow) for the circular cylinder (elip, $\mathrm{AR} = 1.0$).

reference	Re_c
Zebib (1987) [26]	45
Jackson (1987) [7]	46.136
Provansal *et al.* (1987) [4]	47
Strykowski & Sreenivasan (1990) [5]	46
Kumar & Mittal (2006) [27]	47.045-47.3181
Paul *et al.* (2014) [8]	48.325
Thompson *et al.* (2014) [9]	47.2
Chopra & Mittal (2019) [28]	46.985
present study	47.3 ± 0.25

For the square section (Table 2), reported data interval is [45-51.2] while the present value is 45 ± 0.25. Finally, for the front pointing triangle (Table 3), the data are huddled between 39.6 and 40.5 including the present value. The present methodology output is thus in very good agreement with references for three different geometries. This validates the detection of unsteadiness onset by the binary search with the selected monitoring and threshold, combined with the IBM technique in the direct solver, for the study of the influence of shape on this transition. Further validation is provided in Section 3.1 where the influence of aspect ratio is described, using grid refinement for short bodies and additional literature data.

Table 2. Literature values of Re_c (transition from steady to unsteady flow) for the square cylinder (rect, $\mathrm{AR} = 1.0$).

reference	Re_c
Sohankar *et al.* (1997) [29]	47 ± 2
Sohankar *et al.* (1998) [30]	51.2
Saha *et al.* (2000) [31]	> 45
Yoon *et al.* (2010) [32]	45
Bai & Alam (2018) [33]	~ 50
Jiang & Cheng (2018) [34]	~ 46
present study	45.0 ± 0.25

Table 3. Literature values of Re_c (transition from steady to unsteady flow) for the front-pointing triangular cylinder (trif, $\mathrm{AR} = 1.0$).

reference	Re_c
Zielinska & Wesfreid (1995) [35]	39.6
De & Dalal (2006) [36]	39.9
Prhashanna *et al.* (2011) [37]	40 ± 0.5
Ng *et al.* (2016) [38]	40.45
present study	39.8 ± 0.25

3. RELATIONSHIP BETWEEN THE CRITICAL REYNOLDS NUMBER AND AR

The tested geometries here can be separated in two groups: I) the ellipse, front-pointing triangle and rectangle (elip, trif and rect), that follow an exponential law and converge toward the same value for $\mathrm{AR} \to 0$, as visible in Figure 4; II) back-pointing triangle (trib) and lozenge (losn), shown in Figure 5, that have a rather constant Re_c until unitary AR, and an almost identical tendency afterwards.

To model the increase of Re_c with aspect ratio, several laws were tried (see discussion in the A), and the following exponential law has been selected:

$$\mathrm{Re}_c = a \exp(b\mathrm{AR}) \tag{5}$$

The resulting laws are presented in Figure 4 and 5, and the coefficients are listed in Tables 4 and 5 in Appendix A, together with the determination coefficient R^2 and the p-value for a normality test [39] of the error. A high p-value ($\gtrsim 0.05$) means that the null hypothesis that the data came from a normally distributed population can not be rejected. For the elliptical section, for example, coefficients are a = 30.55 and b = 0.4549, with R^2 = 0.99 and normality test p-value = 0.68. Overall, from Figure 4 and 5 and Tables 4 and 5, the proposed model (5) is of very good statistical quality.

3.1 Behavior for short bodies (low AR's)

Unlike for $\mathrm{AR} \geq 1.0$ where the exponential trend appears clearly on the data, the influence of the aspect ratio seems less universal for short bodies. There are indeed two behaviors, as investigated in this section.

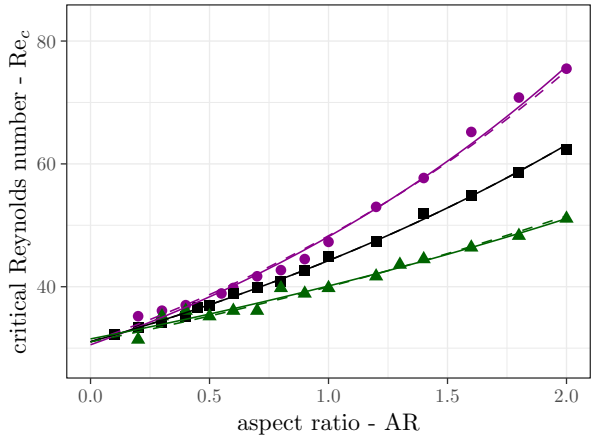

Figure 4. Binary search results (symbols) and regression laws for the critical Reynolds number as a function of the aspect ratio for group I (elip, rect and trif). Solid lines represent the 2 parameters regression while the hashed ones correspond to the laws derived with an imposed $\mathrm{Re}_{c,\mathrm{AR}\to 0}$. For readability, the symbol shape is that of the body for $\mathrm{AR} = 1$, with flow from top to down.

3.1.1 The thin plate as a limit for elip, rect and trif

The congruence of the points and the regression laws at small AR allows the definition of a flat-plate critical Reynolds number ($\mathrm{Re}_{c,\mathrm{AR}\to 0}$). Considering that Equation (5) is exponential, the coefficient a corresponds to this value ($\mathrm{Re}_c = a$ when $\mathrm{AR} = 0$). That leads to the following reduced model:

$$\frac{\mathrm{Re}_c}{\mathrm{Re}_{c,\mathrm{AR}\to 0}} = \exp(b\mathrm{AR}) \tag{6}$$

Considering the average of the 3 shapes on the first group, the critical Reynolds number for a thin plate ($\mathrm{AR} \to 0$) is of 31.03. This value lies within the range of 30-35 proposed by Saha [40] and is very close to that obtained by Thompson *et al.* [9] of 31.6. The values of the regression parameter b when a is thus fixed are given in Table 4, and the reduced models are plotted in Figure 4. The single parameter models (6) are found almost indistinguishable from their two parameter counterpart (5). This establishes the relevancy of the common value when $\mathrm{AR} \to 0$ for the three tested geometries. It is thus evidenced that ellipses, rectangles and front-pointing triangles have the same onset of unsteadiness as a plate normal to the flow when their aspect ratio is close to zero.

3.1.2 Grid refinement

For the lozenge and the back-pointing triangle, the critical Reynolds number seems almost constant for $\mathrm{AR} \leq 1.0$, as visible in Figure 5. However, a dispersion of the data is noticed, in particular for the triangular section. Given the limitations of the present methodology regarding both

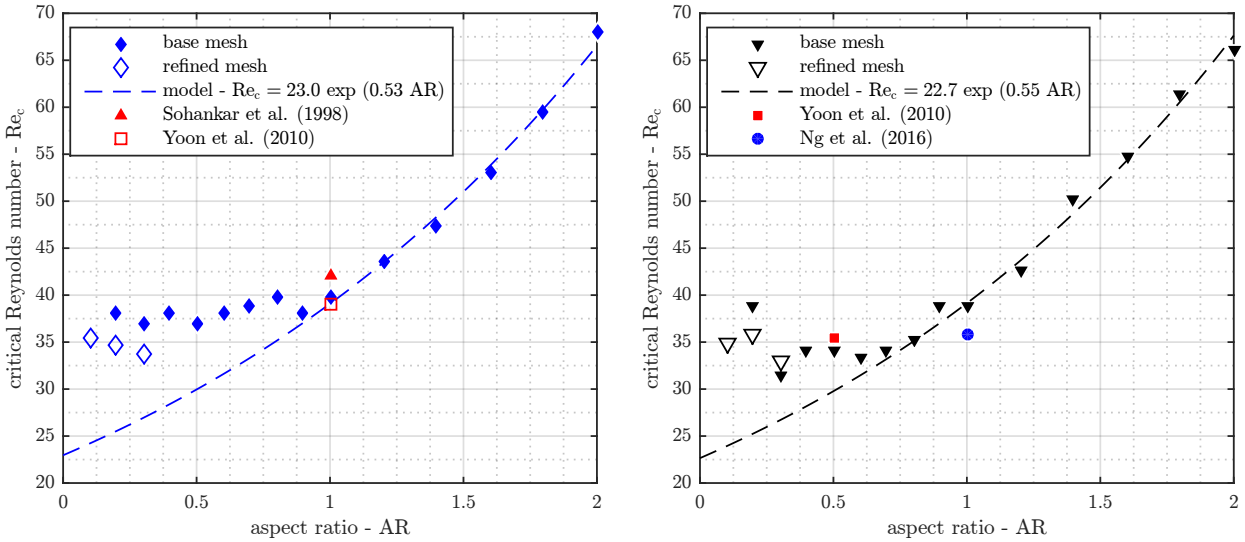

Figure 5. Binary search and literature results (symbols) and regression laws for the critical Reynolds number as a function of the aspect ratio, for lozenge (losn, left) and back-pointing triangle (trib, right). The value for the latter geometry at $\mathrm{AR} = 0.5$ is taken from Figure 15 of the study by Yoon *et al.* [32] on a square cylinder at incidence. Hashed lines represent 2 parameters regression fit calculated for $\mathrm{AR} \geq 1.0$.

the no-slip condition modeling with IBM and the detection of unsteadiness, grid refinement is conducted for the shortest cases. The simulations and the binary search are thus rerun with twice more grid points in each direction, for $\mathrm{AR} = 0.1, 0.2$ and 0.3. The resulting Re_c values are added in Figure 5. For the triangle, the dispersion of the result is reduced with the fine grid, leading to $33 \leq \mathrm{Re}_c \leq 36$ for $\mathrm{AR} \leq 1.0$. For the lozenge, the fine grid simulations returns offset Re_c. However, the new values are still higher than the curve obtained by regression of data for $\mathrm{AR} \geq 1.0$. The critical Reynolds number does not appear strictly constant for $\mathrm{AR} \leq 1.0$ but the increase is very weak between an estimated limit value of ≈ 35 for $\mathrm{AR} = 0$ and $\mathrm{Re}_c \approx 40$ for $\mathrm{AR} = 1.0$. This is still twice slower than for the back-pointing triangle, which has the slowest increase of Re_c with AR in group I.

Note that the present data, even with the coarse grid, are in perfect agreement (same Reynolds number unit) with the values reported by Yoon *et al.* [32] for the lozenge at $\mathrm{AR} = 1.0$ and for the back-pointing triangle at $\mathrm{AR} = 0.5$. Good agreement (2-3 Re units) is also obtained at $\mathrm{AR} = 1.0$ with Sohankar *et al.* [29] for lozenge and Ng *et al.* [38] for the triangle.

Moreover, the grid refinement has been conducted for the ellipse at $\mathrm{AR} = 0.1, 0.2$ and 0.3 and 1.0, enabling further comparison with previously reported data, as visible in Figure 6 and discussed in section 3.2. Less than 2 Re unit difference is noted between the two present grid and between the present and literature data. The values for the finer grid also fall better on the regression curve.

It can thus be concluded that the grid refinement study confirms the results obtained with the coarse grid. Moreover, the uncertainty intervals yielded by the discretization error are consistent with those yielded by the threshold of unsteadiness and the dispersion on Re_c noted in the literature, and small with respect to the whole dynamics of Re_c, which lays over 40 Reynolds number units for $0.2 \leq \mathrm{AR} \leq 2.0$.

3.1.3 Existence of a Re_c *plateau for losn and trib*

As confirmed by the grid refinement study, there exists a plateau of Re_c for back-pointing triangles and lozenges $\mathrm{AR} \leq 1.0$. The lozenge is an intermediate shape between the front- and back- pointing triangles, and this appears to imprint on its onset of unsteadiness through a little increase of Re_c (slopped plateau), while the trif has a stronger increase (no plateau) and the trib a definite plateau. Further computations involving hybrid shapes lead to the conclusion that the plateau is generated by the lateral edge rather than by the downstream edge.

The laws for the two geometries (trib and losn) for $\mathrm{AR} \geq 1.0$ are coincidental and reproduce the exponential behavior noted for group I.

3.2 Comparison with previous studies on aspect ratio

A comparison between the present law along with the values obtained by Jackson [7], Paul *et al.* [8] and Thompson *et al.* [9] is available in Figure 6.

Present results fit well the trend encountered by Jackson [7], and Thompson *et al.* [9], and values given by Paul *et al.* [8] for $1 \leq \mathrm{AR} \leq 2.0$. The later reference reported values that are distant from the other sources for $\mathrm{AR} < 1.0$. It is believed that this offset is due to the difference in the numerical setup associated with using the hydraulic diameter as reference for the domain extension. In the computations by Paul *et al.* [8] for low AR elliptical cylinders, the data and regression law may capture the influence of the increase of the blockage rather than that of the modification of the geometry.

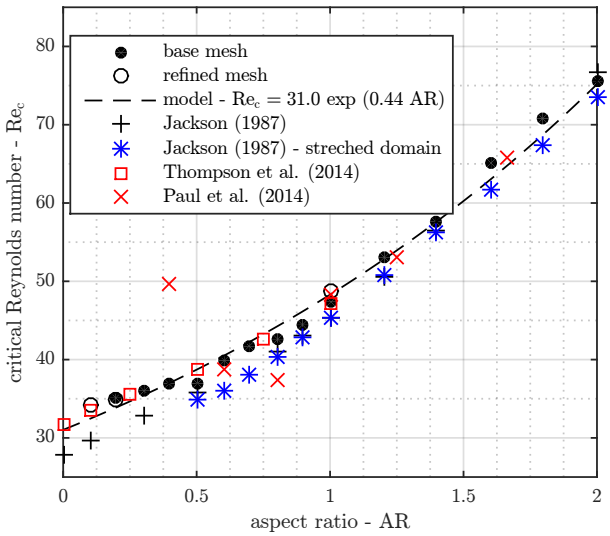

Figure 6. Comparison of the evolution of the critical Reynolds number with the aspect ratio, elliptical section, with literature values [7–9]. The dashed line represents the regression law obtained from current data with an imposed $\mathrm{Re}_{c,\mathrm{AR}\to 0}$.

As for large aspect ratios, a bias due to the transition criteria used in [8] may partly explain why the Re_c reported for $\mathrm{AR} = 10$ is lower than the present exponential law tendency. Present $\mathrm{Re}_c(\mathrm{AR})$ models would lead to an infinite critical Reynolds number with the increase of the aspect ratio (for an infinitely long flat plate parallel to the flow). The existence of a vortex shedding is uncertain for long plates, and a different category of flow, fundamentally defined by boundary layer effects, exists. That behavior is physically plausible, however, more data are necessary to confirm that and the consistency of the extrapolation of the proposed model to extended bodies ($\mathrm{AR} > 2$).

4. CONCLUSIONS

4.1 Summary and brief interpretation of results

The Reynolds number for the steady to unsteady flow transition is estimated for multiple bluff bodies in 2D using a DNS solver. Via a bisection scheme, the Re_c are obtained with a precision of $\pm$ 0.25. Despite the simplicity of the current framework, values fit well with literature for the circular, square, and front-pointing triangle at $\mathrm{AR} = 1.0$, and a database containing 70 geometries is presented. With the use of several aspect ratios, the following global trend is noted:

$$\mathrm{Re}_c = a \exp(b\mathrm{AR}) \tag{7}$$

where $a \approx 31$ is common to all geometries, thus estimating the normal thin plate critical Reynolds number, and $b \approx 0.24 - 0.45$ is specific to each shape.

The elliptical section is the only considered shape that has no sharp edge, and this geometrical feature is attributed to the observed behavior of having the highest critical Reynolds number among the tested cross-sections. The fact that there are no fixed detachment points leave more space for adaptation of the flow within a steady solution. Also, for the ellipses, the boundary layer remains attached over larger perimeters, thus, are capable of provoking more diffusion and releasing vorticity to the flow, thus, need to have a more energetic flow to transition.

4.2 Link with aeroacoustics

A good statistical correlation has been evidenced [12] between the distance to unsteadiness, quantified by ε (see Section 2.3.2), and the lift fluctuation normalized by AR at $\mathrm{Re} = 150$. The present study on Re_c may thus shed light on recent optimization results [19, 20].

4.2.1 Analysis of optimal shapes

Optimal shapes for aeroacoustics has been computed using the same numerical Navier-Stokes solver as the present study. Minimization and maximization of acoustic power has been performed at $\mathrm{Re} = 150$. Two main features are noticed.

Firstly, the aspect ratio is a main driver of the noise for $\mathrm{AR} \geq 1$, since noise minimizations systematically converge to the longest geometry. This is fully consistent with the exponential relationship exhibited in the present computations.

Secondly, for a fixed $\mathrm{AR} = 1.5$, the rectangular section is close to be the least noisy shape, while the back pointing triangle is close to be the most [19]. The least noisy shape is also close to a rectangle when the aspect ratio is left free between 1 and 2 [20]. Taking $\mathrm{AR} = 1.5$, one obtains $\mathrm{Re}_c \sim 53$ from figure 4 for the rectangle and $\mathrm{Re}_c \sim 51$ from figure 5 for the back pointing triangle. These almost equal values can not explain the almost 15 dB difference of acoustic power between rect and trib at $\mathrm{AR} = 1.5$ only by pure difference of level of unsteadiness. Indeed, the formalism scaling fluctuation amplitude on ε is theoretically valid only for small values of ε. The unsteady lift generation should thus rather credited to the spatial organization of the shear-layer flapping in the vicinity of the lifting surface: for the back pointing triangle, the vortices are formed just above the body, while they are pushed downstream it for the rectangle.

4.2.2 Imprint of Re_c *on the noise at* $\mathrm{Re} \approx 20,000$.

Among other cylinders (circular, square, rectangular of $\mathrm{AR} = 2$), the rectangular cylinder of $\mathrm{AR} = 3$ has been measured [15] as the noisiest for $\mathrm{Re} \approx 20,000$ and a Mach number of about 0.1. Moreover, the acoustic peak at the lift frequency was the sharpest. Such an efficient tonal emission has been linked [15, 25] with high levels of spanwise coherence over almost the whole length of the model for this shape at this frequency. Thus, at this regime, the fundamental mode (lift mode) can almost be considered as still two-dimensional (2D), unlike the flow over shorter shapes, square and circular in particular. Such delayed tridimensionalization of the long-breadth shape may be fully consistent with the exponential dependency of the critical

Reynolds number with the aspect ratio that has been obtained presently. Further theoretical study of the influence of shape on 2D-3D transition is needed to confirm this conjecture.

A. REGRESSION LAWS

The coefficients and statistical quantities for the $\mathrm{Re}(\mathrm{AR})$ models in (5) and (6) are given in Tables 4 and 5. Regression model $\mathrm{Re}_c = a + b\mathrm{AR}^2$ was found as statistically significant as the exponential curve that is proposed. For the elliptical section, for example, the determination coefficient is of 0.99 and the p-value of the normality test is of 0.85. However, the parabolic curve does not capture well the tendency at low Reynolds number (a close to linear increase of Re_c with AR) and is less consistent when taking account the completeness of the tested shapes. In Table 5, note how similar are the regression coefficient for $\mathrm{AR} \geq 1$.

B. REFERENCES

[1] A. Roshko, "On the drag and shedding frequency of two-dimensional bluff bodies," tech. rep., National Advisory Committee for Aeronautics, 1954.

[2] A. Roshko, "On the wake and drag of bluff bodies," *Journal of the Aeronautical Sciences*, vol. 22, pp. 124–132, Feb. 1955.

[3] C. H. K. Williamson, "Vortex dynamics in the cylinder wake," *Annual Review of Fluid Mechanics*, vol. 28, no. 1, pp. 477–539, 1996.

[4] M. Provansal, C. Mathis, and L. Boyer, "Bénard-von kármán instability: transient and forced regimes," *Journal of Fluid Mechanics*, vol. 182, p. 1–22, 1987.

[5] P. J. Strykowski and K. R. Sreenivasan, "On the formation and suppression of vortex 'shedding' at low reynolds numbers," *Journal of Fluid Mechanics*, vol. 218, p. 71–107, 1990.

[6] B. Pier, "On the frequency selection of finite-amplitude vortex shedding in the cylinder wake," *Journal of Fluid Mechanics*, vol. 458, p. 407–417, 2002.

[7] C. P. Jackson, "A finite-element study of the onset of vortex shedding in flow past variously shaped bodies," *Journal of Fluid Mechanics*, vol. 182, p. 23–45, 1987.

[8] I. Paul, K. A. Prakash, and S. Vengadesan, "Onset of laminar separation and vortex shedding in flow past unconfined elliptic cylinders," *Physics of Fluids*, vol. 26, no. 2, p. 023601, 2014.

[9] M. C. Thompson, A. Radi, A. Rao, J. Sheridan, and K. Hourigan, "Low-reynolds-number wakes of elliptical cylinders: from the circular cylinder to the normal flat plate," *Journal of Fluid Mechanics*, vol. 751, p. 570–600, 2014.

[10] A. Inasawa, M. Asai, and T. Nakano, "Sound generation in the flow behind a rectangular cylinder of various aspect ratios at low mach numbers," *Computers & Fluids*, vol. 82, no. Supplement C, pp. 148 – 157, 2013.

[11] F. Margnat, "Hybrid prediction of the aerodynamic noise radiated by a rectangular cylinder at incidence," *Computers & Fluids*, vol. 109, pp. 13 – 26, 2015.

[12] W. J. G. S. Pinto, F. Margnat, and Y. Gervais, "Influence of cross-section on the aeolian tone: a numerical study in the laminar regime," in *25th AIAA/CEAS Aeroacoustics Conference (Aeroacoustics 2019), 20-24 May, Delft, The Netherlands*, 2019.

[13] W. King and E. Pfizenmaier, "An experimental study of sound generated by flows around cylinders of different cross-section," *Journal of Sound and Vibration*, vol. 328, no. 3, pp. 318 – 337, 2009.

[14] E. L. Iglesias, D. Thompson, and M. Smith, "Experimental study of the aerodynamic noise radiated by cylinders with different cross-sections and yaw angles," *J. Sound Vib.*, vol. 361, pp. 108 – 129, 2016.

[15] W. J. G. S. Pinto, F. Margnat, and Y. Gervais, "Effect of cross-section on flow three-dimensionality for prismatic bodies and the associated noise emission," in *25th AIAA/CEAS Aeroacoustics Conference*, (Delft, The Netherlands), 20-24 May 2019.

[16] S. U. Islam, C. Y. Zhou, A. Shah, and P. Xie, "Numerical simulation of flow past rectangular cylinders with different aspect ratios using the incompressible lattice boltzmann method," *Journal of Mechanical Science and Technology*, vol. 26, pp. 1027–1041, Apr 2012.

[17] C. Mathis, M. Provansal, and L. Boyer, "The benard-von karman instability: an experimental study near the threshold," *J. Physique Lett.*, vol. 45, no. 10, pp. 483–491, 1984.

[18] C. Norberg, "Flow around a circular cylinder: aspects of fluctuating lift," *Journal of Fluids and Structures*, vol. 15, no. 3, pp. 459 – 469, 2001.

[19] W. J. G. da Silva Pinto and F. Margnat, "A shape optimization procedure for cylinders aeolian tone," *Computers & Fluids*, vol. 182, pp. 37 – 51, 2019.

[20] W. J. G. da Silva Pinto and F. Margnat, "Shape optimization for the noise induced by the flow over compact bluff bodies," *Computers and Fluids*, vol. 198, p. 104400, 2020.

[21] S. Laizet and E. Lamballais, "High-order compact schemes for incompressible flows: A simple and efficient method with quasi-spectral accuracy," *Journal of Computational Physics*, vol. 228, no. 16, pp. 5989 – 6015, 2009.

Table 4. Regression law for the critical Reynolds number as a function of the aspect ratio - group I.

	2 parameters regression - Equation (5)			imposing $\mathrm{Re}_{c,\mathrm{AR}\to 0}$		
geometry	elip	rect	trif	elip	rect	trif
$\log(a)$	3.42	3.44	3.45		3.44*	
a	30.55	31.04	31.50		31.03*	
b	0.455	0.355	0.242	0.442	0.355	0.254
adjusted R^2	0.99	1.00	0.96	1.00	1.00	0.99
Shapiro-Wilk p-value	0.68	0.61	0.12	0.64	0.61	0.04

* Regression performed considering a common Re_c at $\mathrm{AR} = 0$, average of the a coefficients obtained for the 3 shapes.

Table 5. Regression law for the critical Reynolds number as a function of the aspect ratio - group II.

	2 parameters regression - Equation (5)			
	$\mathrm{AR} < 1$		$\mathrm{AR} \geq 1$	
geometry	losn	trib	losn	trib
$\log(a)$	3.61	3.52	3.13	3.12
a	36.80	33.72	22.96	22.65
b	0.0679	0.0702	0.532	0.547
adjusted R^2	0.27	-0.08	0.99	0.99
SW p-value	0.40	0.52	0.15	0.07

[22] D. Goldstein, R. Handler, and L. Sirovich, "Modeling a no-slip boundary condition with an external force field," *Journal of Computational Physics*, vol. 105, pp. 354–366, 1993.

[23] F. Margnat and V. Morinière, "Behavior of an immersed boundary method in unsteady flows over sharp-edged bodies," *Computers and Fluids*, vol. 38, no. 6, pp. 1065–1079, 2009.

[24] Z. Y. Ng, T. Vo, and G. J. Sheard, "Stability of the wakes of cylinders with triangular cross-sections," *J. of Fluid Mech.*, vol. 844, p. 721–745, 2018.

[25] W. J. Gonçalves da Silva Pinto, *Modelling airframe noise : from aerodynamic topology to acoustic efficiency*. Phd thesis, Université de Poitiers, Oct. 2019.

[26] A. Zebib, "Stability of viscous flow past a circular cylinder," *Journal of Engineering Mathematics*, vol. 21, pp. 155–165, Jun 1987.

[27] B. Kumar and S. Mittal, "Prediction of the critical reynolds number for flow past a circular cylinder," *Computer Methods in Applied Mechanics and Engineering*, vol. 195, no. 44, pp. 6046 – 6058, 2006.

[28] G. Chopra and S. Mittal, "Drag coefficient and formation length at the onset of vortex shedding," *Physics of Fluids*, vol. 31, no. 1, p. 013601, 2019.

[29] A. Sohankar, C. Norberg, and L. Davidson, "Low-reynolds-number flow around a square cylinder at incidence: study of blockage, onset of vortex shedding and outlet boundary condition," *Int. J. for Numerical Methods in Fluids*, vol. 26, no. 1, pp. 39–56, 1998.

[30] A. Sohankar, C. Norbergb, and L. Davidson, "Numerical simulation of unsteady low-reynolds number flow around rectangular cylinders at incidence," *Journal of Wind Engineering and Industrial Aerodynamics*, vol. 69-71, pp. 189 – 201, 1997.

[31] A. K. Saha, K. Muralidhar, and G. Biswas, "Transition and chaos in two-dimensional flow past a square cylinder," *Journal of Engineering Mechanics*, vol. 126, no. 5, pp. 523–532, 2000.

[32] D.-H. Yoon, K.-S. Yang, and C.-B. Choi, "Flow past a square cylinder with an angle of incidence," *Physics of Fluids*, vol. 22, no. 4, p. 043603, 2010.

[33] H. Bai and M. M. Alam, "Dependence of square cylinder wake on reynolds number," *Physics of Fluids*, vol. 30, no. 1, p. 015102, 2018.

[34] H. Jiang and L. Cheng, "Hydrodynamic characteristics of flow past a square cylinder at moderate reynolds numbers," *Physics of Fluids*, vol. 30, no. 10, p. 104107, 2018.

[35] B. J. A. Zielinska and J. E. Wesfreid, "On the spatial structure of global modes in wake flow," *Physics of Fluids*, vol. 7, no. 6, pp. 1418–1424, 1995.

[36] K. A. De and A. Dalal, "Numerical simulation of unconfined flow past a triangular cylinder," *International Journal for Numerical Methods in Fluids*, vol. 52, no. 7, pp. 801–821, 2006.

[37] A. Prhashanna, A. K. Sahu, and R. Chhabra, "Flow of power-law fluids past an equilateral triangular cylinder: Momentum and heat transfer characteristics," *International Journal of Thermal Sciences*, vol. 50, no. 10, pp. 2027 – 2041, 2011.

[38] Z. Y. Ng, T. Vo, W. K. Hussam, and G. J. Sheard, "Two-dimensional wake dynamics behind cylinders with triangular cross-section under incidence angle variation," *J. Fluids Struct.*, vol. 63, pp. 302 – 324, 2016.

[39] S. S. Shapiro and M. B. Wilk, "An analysis of variance test for normality (complete samples)," *Biometrika*, vol. 52, no. 3-4, pp. 591–611, 1965.

[40] A. K. Saha, "Far-wake characteristics of two-dimensional flow past a normal flat plate," *Physics of Fluids*, vol. 19, no. 12, p. 128110, 2007.